Electronic Supplementary Material (ESI) for Environmental Science: Processes & Impacts.

Supplemental Information for:

Determination of biphasic core–shell droplet properties using aerosol optical tweezers

Kyle Gorkowski,[1] Neil M. Donahue, [1] Ryan C. Sullivan[1*]

[1]Center for Atmospheric Particle Studies, Carnegie Mellon University, Pittsburgh, PA

[*]Corresponding Author: Ryan C. Sullivan; rsullivan@cmu.edu

Overview

Herein we outline the Mie scattering coefficients for a homogeneous and core–shell droplet used for the WGM position calculations. We plot the dependence of WGM position vs. refractive index, and dispersion. We plot an example of WGM peak grouping. We discuss the simulation bounds used for the error assessment of the homogeneous and core–shell fitting algorithm. We summarize our absolute error and percent error in our fit parameters for both the homogeneous and core–shell algorithm.

Homogeneous Mie Scattering Model

The homogeneous Mie scattering derivation presented in Bohren and Huffman[1] utilizes a slight variation on the notation present in the main text. The Mie size parameter (Eqn. **Error! Reference source not found.**) is defined by particle radius (a) in Bohren and Huffman, where we used the more common particle diameter (d_p) present in the aerosol community. The Mie size parameter (x) is a dimensionless number that relates the circumference of the particle to wavelength of light (λ) incident to it.

$$\chi = \frac{2\pi a}{\lambda} = \frac{\pi d_p}{\lambda} \tag{1}$$

Lorenz-Mie theory then derives the two scattering coefficients of the sphere, a_n and b_n, using Eqn. 2 and Eqn. 3. The refractive index of the surrounding medium is simplified to be one and therefore m is the refractive index of the droplet.

$$a_n = \frac{m\psi_n(m\chi)\,\psi_n'(\chi) - \psi_n(\chi)\,\psi_n'(m\chi)}{m\psi_n(m\chi)\,\xi_n'(\chi) - \xi_n(\chi)\,\psi_n'(m\chi)} \tag{2}$$

$$b_n = \frac{\psi_n(m\chi)\,\psi_n'(\chi) - m\psi_n(\chi)\,\psi_n'(m\chi)}{\psi_n(m\chi)\,\xi_n'(\chi) - m\xi_n(\chi)\,\psi_n'(m\chi)} \tag{3}$$

The solution utilizes the Riccati-Bessel functions which are written below for reference, in Eqns. 4 to 6. J_n and Y_n are Bessel functions of the first and second kind.

$$\psi_n(\rho) = J_{n+\frac{1}{2}}(\rho)\sqrt{\rho\frac{\pi}{2}} \tag{4}$$

$$\chi_n(\rho) = -Y_{n+\frac{1}{2}}(\rho)\sqrt{\rho\frac{\pi}{2}} \tag{5}$$

$$\xi_n(\rho) = J_{n+\frac{1}{2}}(\rho)\sqrt{\rho\frac{\pi}{2}} + Y_{n+\frac{1}{2}}(\rho)\sqrt{\rho\frac{\pi}{2}}\,i \tag{6}$$

The WGMs arise when the denominator of scattering coefficients is equal to zero. Therefore, we set the denominator for each coefficient equal to zero and solve for the optimum x value given a value of m. The transverse magnetic resonance comes from a_n (Eqn. 7) and the transverse electric resonance comes from b_n (Eqn. 8).

$$0 = m\psi_n(m\chi)\,\xi_n'(\chi) - \xi_n(\chi)\,\psi_n'(m\chi) \tag{7}$$

$$0 = \psi_n(m\chi)\,\xi_n'(\chi) - m\xi_n(\chi)\,\psi_n'(m\chi) \tag{8}$$

The initial guess for the numerical solver for Eqn. 7 or Eqn. 8 is from the analytical solution for the same equations. The analytical solution is presented in Schiller (1993).

Core–Shell Mie Scattering Model

The core–shell solution for the Mie scattering derivation is presented on page 183 in Bohren and Huffman[1]. We used a slightly different notation than presented in Bohren and Huffman[1] with the first change being using subscripts of *c* and *s* in replace of 1 and 2 for the core and shell refractive index, respectively. The shell size parameter is still defined by the total droplet diameter (Eqn. 9), in this case the shell d_p. In Bohren and Huffman[1] the size parameter of the core (y) was defined by the core diameter, whereas we chose to relate it as a fraction of the shell diameter, as shown in Eqn. 10.

$$\chi = \frac{\pi \mathrm{d}_{\mathrm{p-shell}}}{\lambda} \tag{9}$$

$$y = \chi f_c = \frac{\pi \mathrm{d}_{\mathrm{p-core}}}{\lambda} = \frac{\pi \mathrm{d}_{\mathrm{p-shell}} f_c}{\lambda} \tag{10}$$

With these slight notation changes we then write out the scattering coefficients for the core-shell system Eqn. 11 and Eqn. 12.

$$a_n = \frac{\psi_n(\chi)[\,\psi_n'(m_s\chi) - A_n\,\chi_n'(m_s\chi)] - m_s\psi_n'(\chi)[\,\psi_n(m_s\chi) - A_n\,\chi_n(m_s\chi)]}{\xi_n(\chi)[\,\psi_n'(m_s\chi) - A_n\,\chi_n'(m_s\chi)] - m_s\xi_n'(\chi)[\,\psi_n(m_s\chi) - A_n\,\chi_n(m_s\chi)]} \tag{11}$$

$$b_n = \frac{m_s\psi_n(\chi)[\,\psi_n'(m_s\chi) - B_n\,\chi_n'(m_s\chi)] - \psi_n'(\chi)[\,\psi_n(m_s\chi) - B_n\,\chi_n(m_s\chi)]}{m_s\xi_n(\chi)[\,\psi_n'(m_s\chi) - B_n\,\chi_n'(m_s\chi)] - \xi_n'(\chi)[\,\psi_n(m_s\chi) - B_n\,\chi_n(m_s\chi)]} \tag{12}$$

The two terms A_n and B_n contain the influence from the core and are written in Eqn. 13 and Eqn. 14.

$$A_n = \frac{m_s\psi_n(m_s\chi f_c)\psi_n'(m_c\chi f_c) - m_c\psi_n'(m_s\chi f_c)\psi_n(m_c\chi f_c)}{m_s\chi_n(m_s\chi f_c)\psi_n'(m_c\chi f_c) - m_c\chi_n'(m_s\chi f_c)\psi_n(m_c\chi f_c)} \tag{13}$$

$$B_n = \frac{m_s\psi_n(m_c\chi f_c)\psi_n'(m_s\chi f_c) - m_c\psi_n(m_s\chi f_c)\psi_n'(m_c\chi f_c)}{m_s\chi_n'(m_s\chi f_c)\psi_n(m_c\chi f_c) - m_c\psi_n'(m_c\chi f_c)\chi_n(m_s\chi f_c)} \tag{14}$$

The WGMs arise when the denominator of scattering coefficients is equal to zero Eqn. 15 and Eqn. 16. Therefore, we set the denominator for each coefficient equal to zero and solve for the optimum x. The numerical solver starts at the solution to the homogeneous case (f_c=1) and then slowly decreases f_c by steps of 10^{-4}. This is the same approach used to find the WGM resonances in Stewart et al.[3]

$$0 = \xi_n(\chi)[\,\psi_n'(m_s\chi) - A_n\,\chi_n'(m_s\chi)] - m_s\xi_n'(\chi)[\,\psi_n(m_s\chi) - A_n\,\chi_n(m_s\chi)] \tag{15}$$

$$0 = m_s\xi_n(\chi)[\,\psi_n'(m_s\chi) - B_n\,\chi_n'(m_s\chi)] - \xi_n'(\chi)[\,\psi_n(m_s\chi) - B_n\,\chi_n(m_s\chi)] \tag{16}$$

Whispering Gallery Mode Dependence on Refractive Index

The variation of the whispering gallery modes (WGMs) as a function of the refractive index and dispersion are plotted in Figure 1 and Figure 2. The inverse of the average slope for the WGMs was then calculated to get the dependence of each droplet parameter on the WGM resonance. These are presented in the main text for a homogeneous droplet as follows a change of 0.66 nm d_p/cm^{-1}, 0.000095 (m_0)/cm^{-1}, and 0.004 µm (m_1)/cm^{-1}.

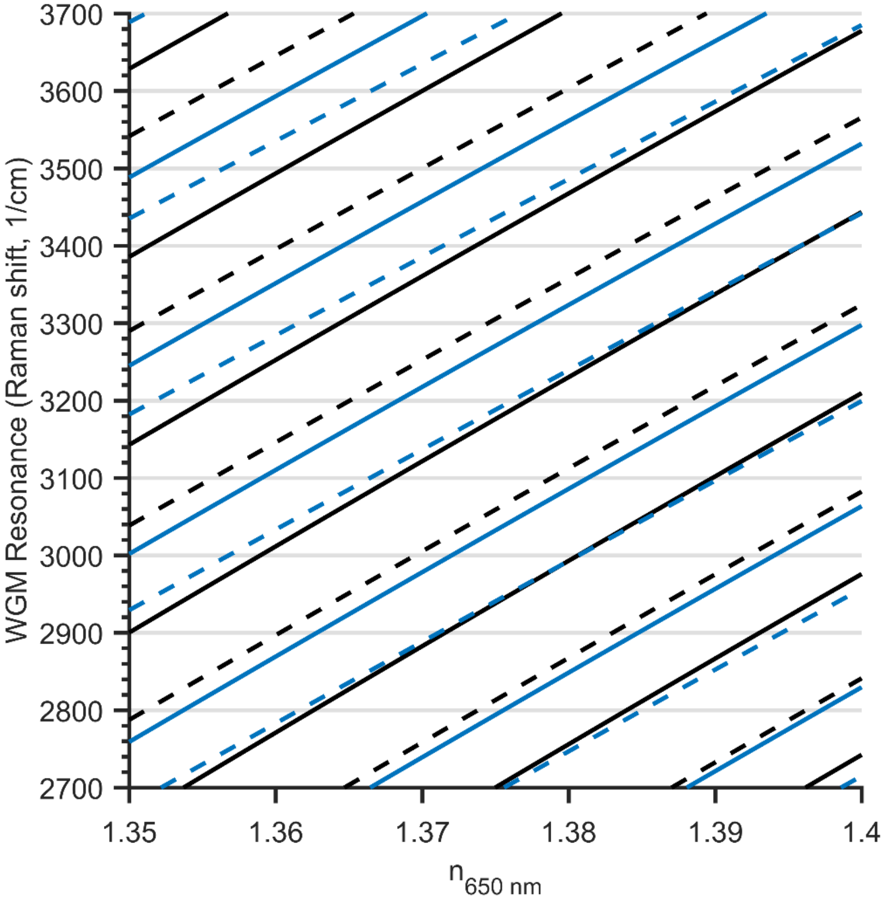

Figure 1. Homogeneous droplet refractive index ($n_{650\ nm}$) variation from 1.35 to 1.4, while keeping the diameter (10 µm) and dispersion constant (0.01 µm). The WGM resonance wavelength is converted to a 532 nm Raman shift, as this is comparable to the AOT measurements. WGM labels are indicated by TE for transverse electric (black) and TM for transverse magnetic (blue), with mode order 1 shown as solid-lines and mode order 2 as dashed-lines.

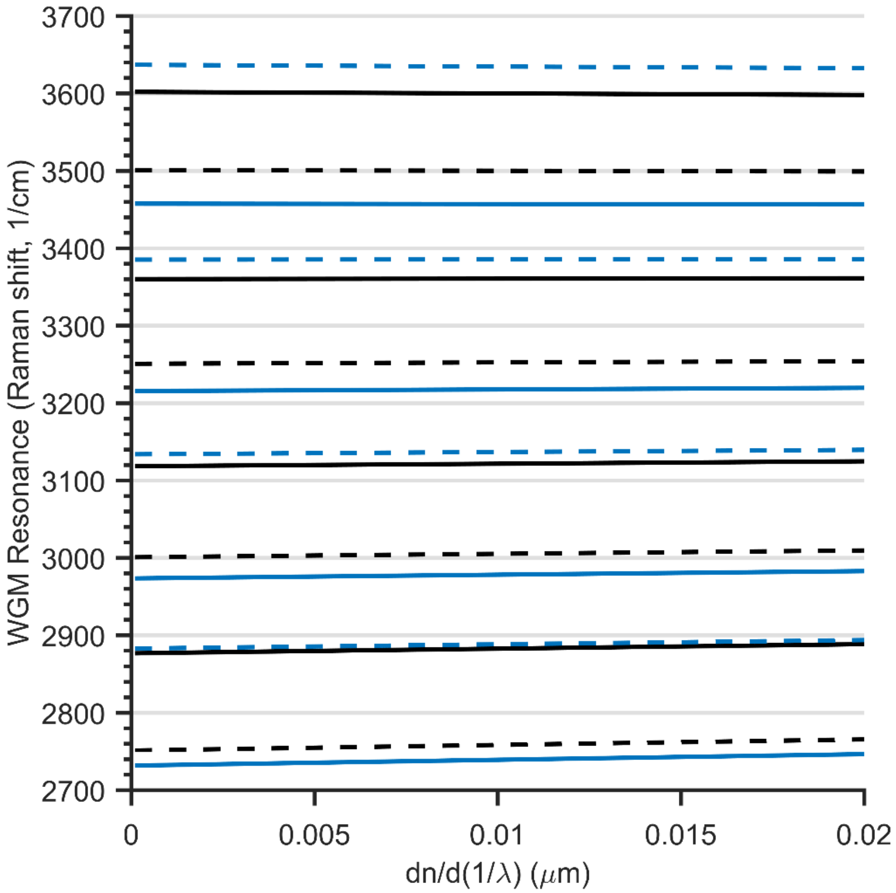

Figure 2. Homogeneous droplet dispersion variation from 0 to 0.02, while keeping the diameter and $n_{650\text{ nm}}$ constant. The WGM resonance wavelength is converted to a 532 nm Raman shift, as this is comparable to the AOT measurements. WGM labels are indicated by TE for transverse electric (black) and TM for transverse magnetic (blue), with mode order 1 shown as solid-lines and mode order 2 as dashed-lines.

WGM Sequence Sorting Example

The sorting of the individual WGMs into sequences follows a simplified version of clustering where if a WGM's position lies within 4 cm^{-1} and the time gap is smaller than 1 minute the next WGM is placed in the same sequences. If the Raman shift (cm^{-1}) or time gap between the previous WGM and the next is larger than that then a new WGM sequences is created. We then remove all the WGM sequences that have less than 30 data points, which helps to remove the scattered WGMs that arise from noise in the data. The result of this sorting is shown in **Figure 3**.

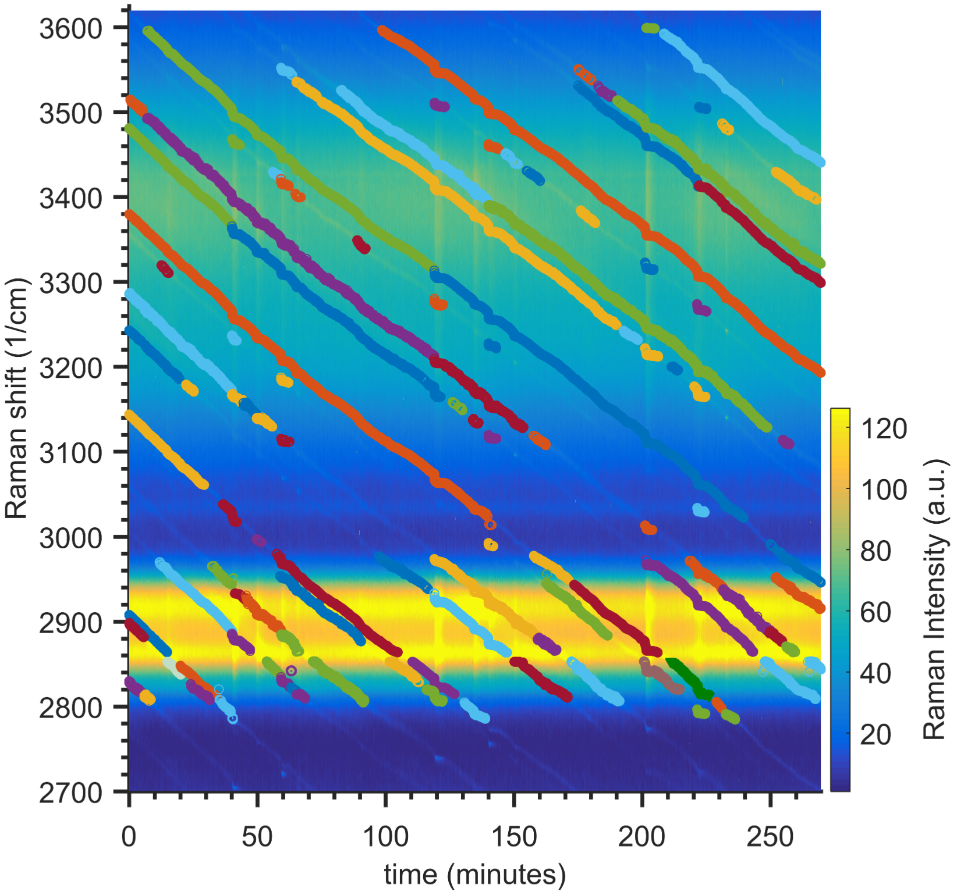

Figure 3. WGM sequences from the squalane coating a glycerol core experiment. There are 111 separate sequences. Each sequence either has a temporal or spectral gap of 1 min or 4 cm^{-1} and by necessity the individual colors are repeated. The C–H hydrocarbon Raman mode center is at 2900 cm^{-1}, the O–H aqueous mode is at 3450 cm^{-1}, and the color scale indicates the intensity of the Raman signal at that Raman shift position.

Additional WGM Simulation Metrics

The dispersion fit error is plotted in Figure 4, showing that with the fewer parameters in the Homogeneous fit the dispersion parameter is more constrained than in the core–shell fit.

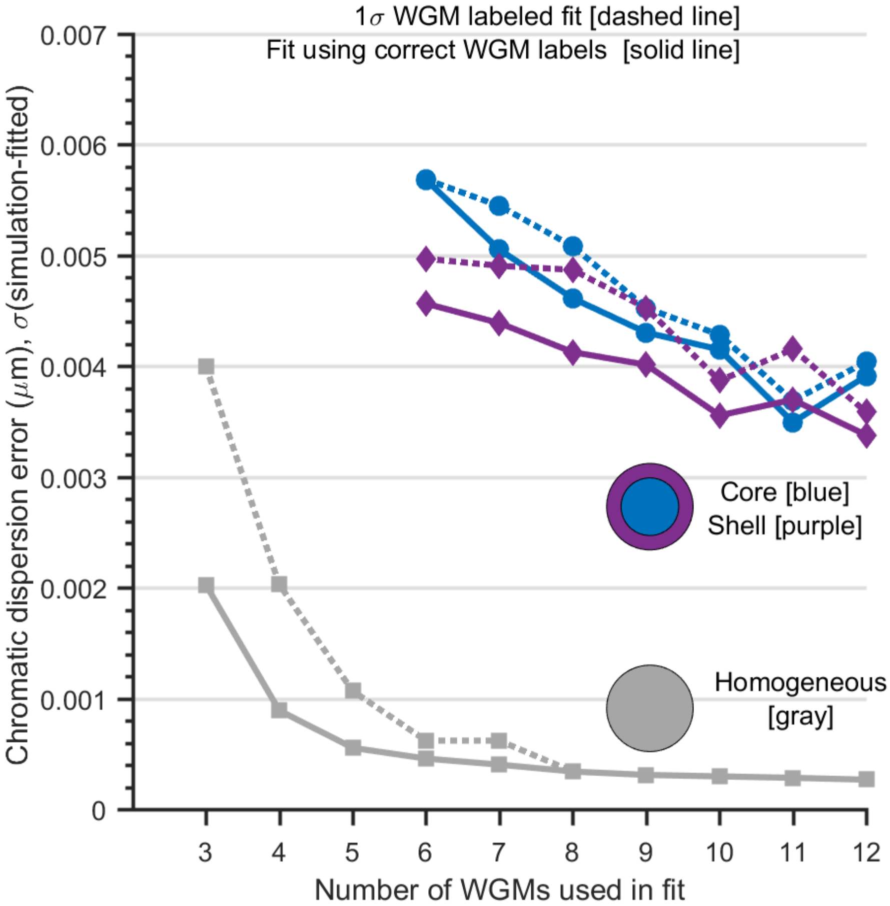

Figure 4. The chromatic dispersion (m_1) fit error of homogeneous and core–shell WGMs versus the number of WGMs used. The standard deviation is for 300 simulated droplets at each set of WGMs used. The dashed line represents the mean of all the fits within 1σ of the global minimum. The solid line is the minimum using the correct WGM labels.

The outline of the algorithm is shown in Figure 5. The inputs to the algorithm are the full time-series of the WGM positions and the standard deviations (σ) of the Gaussian fits for each WGM peak. The full fitting of an experimental time-series starts in the dark green box in the upper left corner and follows the thin green arrows. The WGM labeled fit exits its loop after the WGMs are all labeled and then follows the thick green arrows to the bottom right green box, i.e. the end point. The 1σ WGM labeled fit (or isolated frame analysis) follows the thick orange arrows starting in the upper left and ending in the lower right of Figure 5.

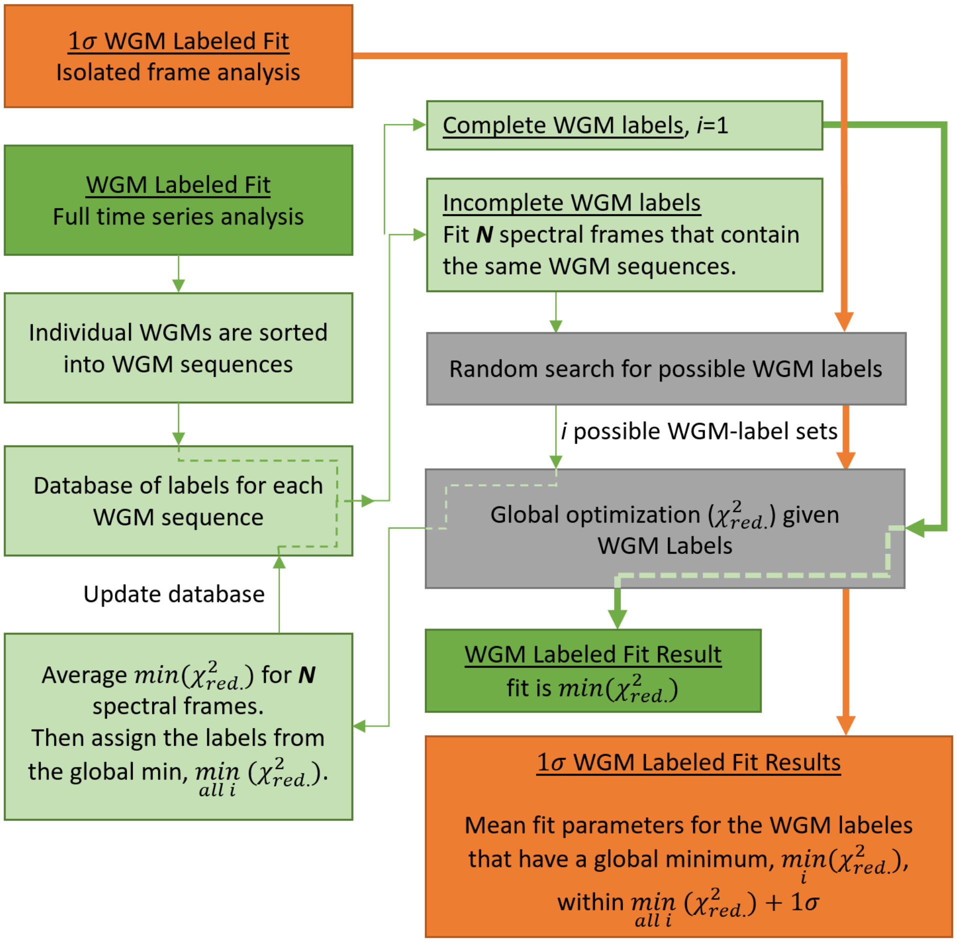

Figure 5. Computational outline for the fitting algorithm. Orange represents 1σ WGM labeled fit which uses only a single frame analysis. The green path represents the preferred way to analysis a full time-series using the method of WGM grouping.

The average computational times for each part of the algorithm are broken down in **Table 1**. The cluster of 32 CPUs has two disadvantages when compared the CPU+GPU method. The first being network communication which we contribute to the major slow-down for the time per random draw, as that step requires frequent communication between the parallel nodes. That could be improved with a more hierarchical splitting of the parallelization. The second drawback is that the GPU is much faster at the large matrix operation used in the global optimizations than the CPU. Even though the cluster's global optimization is efficiently parallelized (no node interdependence) across the cluster of 32 cores, the GPU is more efficient.

Table 1. Summary of computational times for the fitting algorithm.

	Homogeneous Droplet (CPU only)	**Core–Shell Droplet (CPU + GPU)**	**Core–Shell Droplet (32 CPUs)**
Time per random draw for WGM labels	22 ms	0.7563 sec	2.541 sec
Global optimization time per set of WGM labels	9 ms	0.576 sec	0.949 sec
Total time per set of unlabeled WGMs	2.6 sec	6.82 min	15.52 min

The simulation bounds for the error assessment for the homogeneous and core–shell fits are shown in Table 2. For the error assessment 300 individual droplets were randomly generated within the bounds listed in Table 2.

Table 2. Simulation bounds for the error assessment of the fitting algorithm.

	Homogeneous Simulation	Core–Shell simulation
m_{C0} (n_{650nm})	1.37 to 1.42	1.37 to 1.42
m_{S0} (n_{650nm})	-	1.4 to 1.45
m_{C1} (dispersion)	0 to 0.02 µm	0 to 0.02 µm
m_{S1} (dispersion)	-	0 to 0.02 µm
d_p or $d_{p\text{-shell}}$	9 to 11 µm	9 to 11 µm
f_c (fraction of core)	-	0.8 to 1

The WGM dependent error curves present in the main text Figure 4 and Figure 5 were averaged over the typical number of WGMs observed. This would be 5 to 12 WGMs for the homogeneous droplets and 8 to 12 WGMs for the core–shell droplets. The mean absolute error and the relative error are presented in Table 3.

Table 3. Simulation bounds for the error assessment of the fitting algorithm.

	Homogeneous Simulation		**Core-Shell simulation**	
	Mean of STDV error	Mean of Percent Diff.	Mean of STDV error	Mean of Percent Diff.
m_{C0} (typically n_{650nm})	0.000670	0.0582%	0.00508	0.365%
m_{S0} (typically n_{650nm})	-	-	0.00601	0.371%
m_{C1} (dispersion)	0.0000364 µm	20.0%	0.00409 µm	64.1%
m_{S1} (dispersion)	-	-	0.00375 µm	144%
d_p or $d_{p\text{-shell}}$	4.64 nm	0.0456%	24.7 nm	0.242%
$d_{p\text{-core}}$	-	-	356 nm	3.87%
f_c (fraction of core)	-	-	0.0340	3.76%

Method for α-Pinene SOA Addition

The method we implemented for α-pinene secondary organic aerosol (SOA) addition turns the AOT chamber into a flow reactor; the experimental schematic is shown in Figure 6. During a typical ozonolysis experiment, the ozone concentration in the AOT was constant at 3.4 ppm_v, calculated based on the air flow rates and volume mixing. The ozone flows from a UV lamp ozone generator (using air) and the output concentration was validated with an ozone monitor (Dasibi 1008-PC). We introduced the α-pinene vapor *via* a second dry air flow (0.05 Lpm) that passed over a pool of liquid α-pinene before entering a secondary port on the top of the mixing chamber. The α-pinene concentration in the mixing chamber was 182 ppm_v, estimated based on temperature, compound saturated vapor pressure, and gas flow rates. In contrast to our previously reported AOT SOA experiments the concentrations are much lower so we do not observe any optically detectable particles from the α-pinene oxidation in the form of small-particle light scattering events in the visual droplet imaging.[4] The vapors and particles produced in the upper section of the AOT chamber were then transported toward the tweezed droplet at the bottom of the AOT chamber. An appreciable portion of the less volatile SOA components was likely lost by adsorption to the metal chamber walls, but these components by necessity will also be present in the nucleated particles that coalesced with the tweezed droplet.[5]

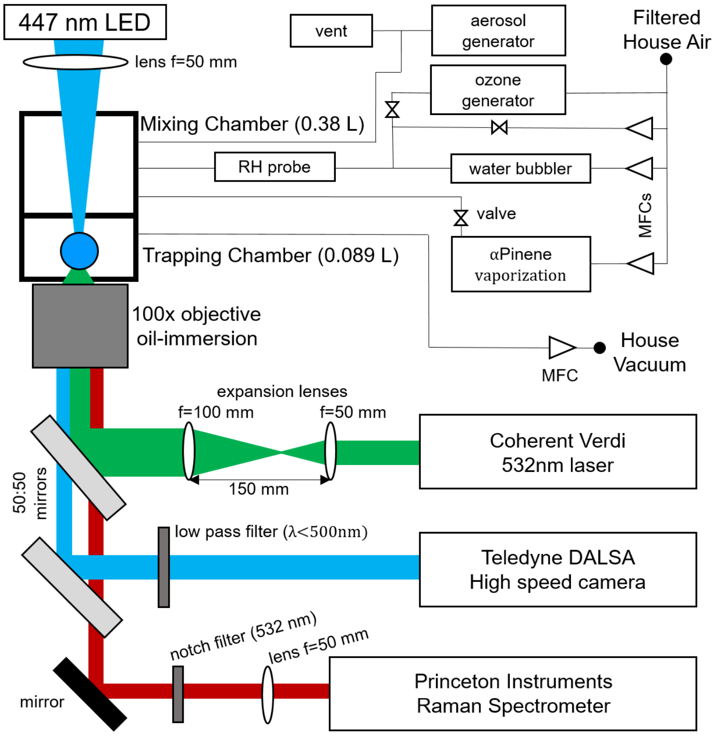

Figure 6. Airflow and optical schematic for the aerosol optical tweezers. The house air is dried and filtered before the mass flow controllers (MFCs, 0-1 LPM). There is a dedicated flow for the introduction of α-pinene vapor that goes directly to the mixing chamber. The RH is controlled by mixing a dry airflow with humid air that has passed through a water bubbler. A hygrometer (Vaisala) measures the T and RH of the conditioned airflow before it enters the upper mixing chamber. There is the option to flow dry airflow form an UV lamp ozone generator. The aerosol generator used is a medical nebulizer if using aqueous solutions, or a Condensational Monodisperse Aerosol Generator (CMAG; TSI, Inc.) to produce large organic droplets. The trapping laser (Coherent Verdi 4 W, 532 nm laser) is expanded to fill the back aperture of the objective, which forms the optical trap. The laser is typically operated at 60 to 200 mW, depending on droplet size. The droplet is backlit using a 447 nm LED and imaged using a Teledyne DALSA high-speed camera. The inelastically scattered light from the droplet is filtered and then recorded with a Princeton Instruments Acton Raman Spectrometer.

Supplementary References

1 C. F. Bohren and D. R. Huffman, *Absorption and Scattering of Light by Small Particles*, Wiley-VCH Verlag GmbH, Weinheim, Germany, 1998.

2 S. Schiller, Asymptotic expansion of morphological resonance frequencies in Mie scattering., *Appl. Opt.*, 1993, **32**, 2181–2185.

3 D. J. Stewart, C. Cai, J. Nayler, T. C. Preston, J. P. Reid, U. K. Krieger, C. Marcolli and Y. H. Zhang, Liquid–Liquid Phase Separation in Mixed Organic/Inorganic Single Aqueous Aerosol Droplets, *J. Phys. Chem. A*, 2015, **119**, 4177–4190.

4 K. Gorkowski, N. M. Donahue and R. C. Sullivan, Emulsified and Liquid–Liquid Phase-Separated States of α-Pinene Secondary Organic Aerosol Determined Using Aerosol Optical Tweezers, *Environ. Sci. Technol.*, 2017, **51**, 12154–12163.

5 N. M. Donahue, A. L. Robinson, E. R. Trump, I. Riipinen and J. H. Kroll, in *Atmospheric and Aerosol Chemistry*, eds. V. F. McNeill and P. A. Ariya, Springer Berlin Heidelberg, Berlin, Heidelberg, 2014, pp. 97–143.